A Compact Series Elastic Actuator for Bipedal Robots with Human-Like Dynamic Performance

Michael David Taylor

CMU-RI-TR-11-31

*Submitted in partial fulfillment
of the requirements for the degree of
Master of Science in Robotics*

Robotics Institute
Carnegie Mellon University
Pittsburgh, Pennsylvania 15213

August 2011

Masters Committee:
Hartmut Geyer
Ralph Hollis
Eric Whitman

© Michael David Taylor 2011

Abstract

Series-elastic actuation offers several important benefits to dynamic robots, including high-bandwidth force control and improved safety. While this approach has become common among legged robots, the lack of commercial series-elastic actuators and the unique design requirements of these robots leaves custom-built actuators as the only option. These custom actuators are often designed for nominal behavior rather than an extended performance envelope, and thus lack the capacity for high dynamic behavior and large-scale disturbance rejection outside of controlled operating conditions. This paper details the design and construction of a compact series elastic actuator for use in the knee of a robotic biped built to emulate the dynamic performance of a half-scale human. The actuator specifications are defined by the combined performance envelope of scaled human knee extensor muscles. The design uses two DC motors geared in parallel for improved weight, compactness, and power density. The constructed actuator is designed for a no-load speed of 210 rpm and a nominal torque of 13 Nm. In addition, a unique approach to series-elastic actuator torque control is proposed which uses servo-controlled motor velocity to modulate spring deflection. Several key advantages of our proposed method over traditional torque-embedded control are demonstrated, including increased torque bandwidth, rejection of nonlinear effects from gear dynamics, and zero steady-state error.

Acknowledgements

Contents

List of Figures

List of Tables

1 Introduction

Our research group's goal is to develop high-performance legged systems using technology that transfers to rehabilitation robotics. It is our hope that our research will realize improved prostheses and orthoses for humans that greatly surpass the limited performance of presently-available assistive devices. This goal poses many challenges and constraints.

First among these challenges is the need to develop devices capable of closely matching the dynamic performance of an unimpaired human. This challenge is twofold: we must understand human dynamics as well as reproduce them in simulation and hardware. We begin by investigating simplified models for walking and running gaits such as the inverted pendulum and spring-loaded inverted pendulum [10]. We also use our knowledge of the human muscoloskeletal system and simplified muscle models to generate a reflexive neuromuscular model for walking [11]. By taking inspiration and guidance from biology in this way, our goal is to reproduce human-like gaits that exhibit stable and adaptive control over uneven terrain and under large disturbances.

With the goal of high-performance dynamic behavior comes a need for precise force feedback and control. Many traditional actuator technologies such as geared electric motors and hydraulics have a high impedance which can make robust force control a difficult problem. It has been shown that an elastic element in between a traditional "stiff" actuator (such as a highly-geared electric motor) and its load can decouple the actuator inertia from the load inertia, allowing for more precise impedance control [1]. If the characteristic force-length curve is known for the compliant element, then the force can be directly inferred by measuring its displacement. Thus, the series-elastic actuator (SEA) force can be controlled by modulating the deflection of the compliant element [1]. Usually this element is either a linear or rotary spring with a constant stiffness, which simplifies the control design. A conceptual diagram of an SEA is given in Figure 1.

An additional benefit of compliant actuation is safety for both the device and its environment. Collisions with a large industrial robot arm have the potential to be disastrous, even if the robot can quickly detect an increase in joint torques and turn itself off. The massive inertia of the robot arm will almost instantaneously transfer large quantities of energy to any object that it rigidly collides with. Compliant elements, even when completely passive, can improve the outcome of such a collision by decoupling the inertia from the site of impact [4]. A properly-selected compliant element will absorb a large amount of the energy, and by spreading the impulse of the collision across a larger time, the maximum force exerted on the object will be reduced. Lower impact torques within the actuator allows the engineer to choose lighter, more compact drive train components such as gears

and bearings.

1.1 Series Elastic Actuator Designs

In the next two subsections, we review the state-of-the-art in SEA design and control.
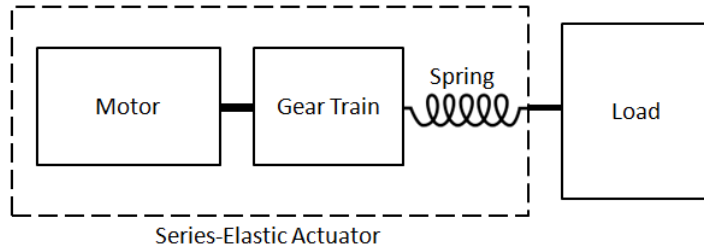
Figure 1: Conceptual diagram of series elastic actuator, adapted from Pratt and Williamson [1]

.

The lack of commercially-available series-elastic actuators means that most are custom-built for specific applications. The design of an SEA includes base actuator selection (usually an electric motor), any stiff transmission components such as a gearbox or spindle drive, and the compliant element itself. Additionally, a sensor capable of measuring the deflection of the compliant element is necessary to implement closed-loop control. The only well-known example of series elastic actuators that could be purchased directly were previously available from Yobotics (shown in Figure 2). The Yobotics linear actuator uses a ball screw assembly and compression springs to exert forces of 556 N at 0.27 m/s. As we will show in the design constraints section of this paper, we would require a linear actuator force of 750 N at a speed of 0.68 m/s to achieve our desired performance, which is outside of the performance range of compact spindle-drive transmissions.
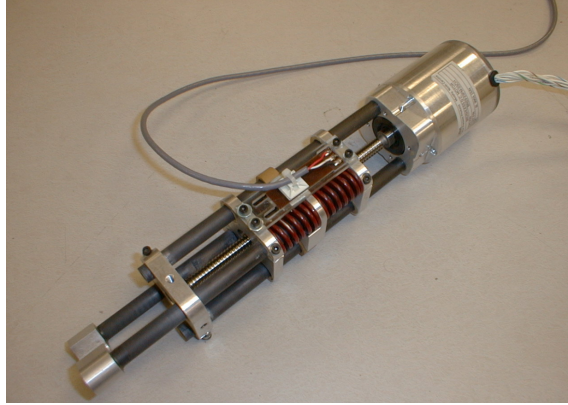
Figure 2: Series elastic actuator previously available from Yobotics. The mechanical transmission includes a ball screw and a linear potentiometer for deflection measurement [17]

.

One recent example of a custom-built SEA that reflects the state-of-the-art in SEA design is the work of Kong et al., who have designed series elastic actuators for use in assistive exoskeletons [5]. These actuators are compact and highly geared. The compliant element is a rotary spring, as opposed to the compression springs used in the Yobotics actuators. The rotary spring has an integrated hard stop, which means that past a certain deflection the motor becomes rigidly coupled to the joint. The design, seen in Figure 3, is also notable in that there is an additional gear stage between the elasticity and the load, though this additional bevel gear pair redirects the direction of rotation without speed reduction.
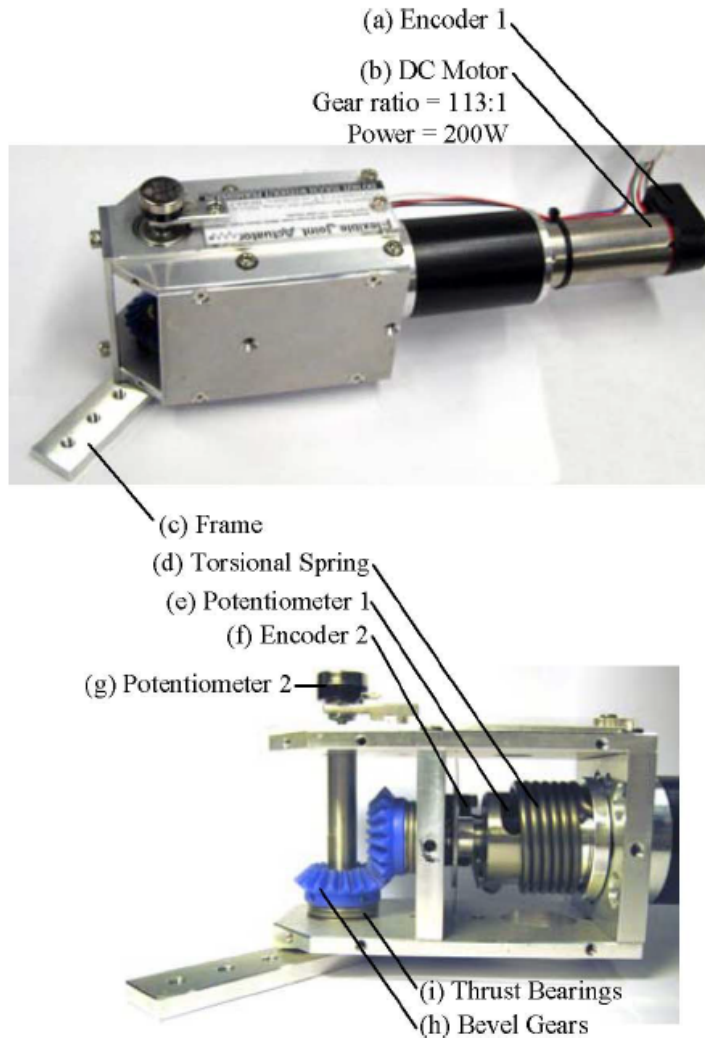
Figure 3: SEA used in a lower-limb assistive device. A planetary gearhead is used as the primary mechanical transmission, with rotary potentiometers used to detect actuator position and spring deflection [5]
.

Several recent SEA designs include mechanically-variable compliance, such as the actuator developed by Hurst et al. shown in Figure 4. As the variable compliance constitutes an additional degree of freedom, designs such as this typically contain at least two motors and are more mechanically complex than fixed-compliance devices. Adjustable compliance allows the burden of impedance control to be shifted from software to hardware, as the natural impedance of the

actuator can be matched to the task at hand. At the cost of increased mechanical complexity, the actuator presented by Hurst et al. has greatly decreased bandwidth limitations which enables highly dynamic legged locomotion [16].
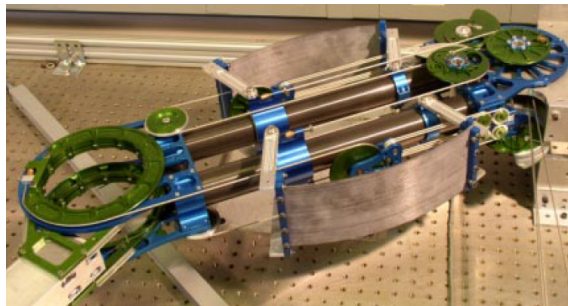
Figure 4: Adjustable-compliance SEA designed for highly dynamic legged locomotion. A high-speed cable drive is used for the mechanical transmission, with variable-radius spiral pulleys enabling various spring engagement ratios [16]

.

While the fundamental concept of SEAs remains relatively constant, the three design examples just described show that the mechanical design space for these actuators is quite large.

1.2 Control Methods for Series Elastic Actuators

Just as SEAs pose unique mechanical design challenges, so too do they require unique control methods. Pratt and Williamson first outlined the benefits of series-elastic actuators, and proposed a basic control architecture which uses current regulation of a DC motor to modulate actuator force [1]. The controller consists of a PID controller and several inverse dynamics terms that describe and compensate for the force required a) to accelerate the motor inertia to track the load motion, b) to accelerate the motor inertia to deflect the spring, and c) to maintain a desired steady-state torque at the output. The inverse dynamics terms assume precise knowledge of the force/deflection constant of the elastic element, as well as knowledge of the motor and drive train rotational inertia. Additionally, these terms do not account for gear friction. If the spring and motor are not well characterized, or if significant friction is present in the drive train, then a greater load will be placed on the PID controller to compensate for torque errors. Because it is a widely used control method, we use this approach as a reference for controlling our series elastic actuator. A more detailed explanation can be found in the Control section of this paper.

5

Some researchers [9] have also explored series damped actuators (SDAs) as an alternative to SEAs. These actuators have a linear damper in series between a stiff actuator and the load. The damper behaves similarly to the spring, except it generates a force in response to its velocity differential rather than its deflection. The damper reduces the order of the system by one and allows for stable force control. Very low impedances are possible for low velocities, while at higher velocities the SDA impedance will approach that of the stiff actuator. One major drawback for the practical application of SDAs, however, is the fact that the damper dissipates energy rather than storing it like a spring. This can lead to greatly reduced efficiency unless the damping coefficient can be controlled.

Hurst et al. state that the primary issue with traditional series elastic actuators is that they only perform well when (A) the load inertia is large compared to the motor's reflected inertia and (B) the motor can produce very high torques with high fidelity [7]. If these conditions are false, then an impulse applied to the load can cause high-frequency oscillations and instability. Hurst and Rizzi argue that these conditions do not generally hold for many robotic applications, and as such, they recommend designing an actuator with an additional damper placed in parallel with the spring. For low load inertias, the damper prevents unwanted oscillations. The damper should be selected such that the actuator is critically damped for the lowest expected load. Hurst et al. show that the damped series elastic actuator reaches steady state force control faster than even an SEA with properly matched impedances [7]. Additionally, contact chatter is greatly reduced. One disadvantage is that the impact forces applied by the actuator are significantly higher than those of a standard SEA, though less than those applied by a traditional stiff actuator. While this characteristic reduces some of the safety benefits of series elasticity, this method has been shown to reduce oscillatory behavior and increase force bandwidth.

Other researchers have sought to improve the fundamental torque-embedded control architecture by adding control structures that predict and reject disturbances and nonlinearities. The control architecture for the human-safe rotary SEA, presented by Kong et al. [5], uses the disturbance observer (DOB) approach to precisely exert a desired force on an orthotic joint. Additionally, Kong et al. distinguish between two distinct modes of operation: when the leg is in contact with the ground, and when it swings freely. These two modes represent drastically different load impedances. For dynamic walking and running robots, a robust controller must be able to command forces and torques in both cases. The method proposed in [5] compensates for disturbances and varying load cases by using an empirically-derived model of the physical system's behavior.

A recent control method proposed by Wyeth relies on an inner motor velocity control loop rather than the current loop used by Pratt and Williamson [3].

Commanding DC motor velocity rather than torque provides a key advantage in that there are no velocity "losses" through a drive train, i.e. the velocity at the output of the drive train is exactly scaled from motor velocity by the gear ratio. In this way, unmodeled torques due to gearbox friction are compensated for by the fast inner control loop, and specific knowledge of motor inertia is not necessary. Wyeth's control method eliminates two of the major sources of error in traditional torque-embedded control, which leads to improved system performance [4]. However, a major disadvantage of this control scheme is that requires explicit knowledge of the load dynamics, which in Wyeth's case have been assumed to be constant and purely inertial. While this formulation with known load dynamics may be useful for industrial robot arms, it is unacceptable for dynamic legged systems, as the load dynamics constantly change due to joint position and gait phase (ground contact vs. free swing). To overcome this limitation, we develop a control method in Section 4 that provides the benefits of velocity control without explicitly specifying load dynamics.

1.3   Summary

While many researchers have explored series elastic actuators, there remain many unexplored possibilities in both design and control. From previous work, however, we identify several important factors that we consider when developing our own unique solutions. In terms of mechanical design, we acknowledge that no ready-made actuator solution exists, which necessitates our own custom design. Most previous actuators use electric motors, for which position, velocity, and current control are all solved problems. Additionally, we see that low reflected inertia, low gear friction, and backdriveability contribute to effective force and torque control. Because of the wide range of applications and operating conditions for series elastic actuators, we see a similarly wide range of control methods, each specifically chosen to fit a given context. It is important that we choose a control method which is well-suited to high-performance legged dynamics. Our method must be able to provide high-bandwidth force control without an explicit model for load dynamics, and must be able to operate at high frequencies and torques characteristic of human joint performance. Both the mechanical design and control method must be able to provide precise force control during swing phase (low impedance) and stance phase (high impedance), and must respond quickly and smoothly during leg touch-down impacts.

7

2 Actuator Design and Fabrication

In order to test current and future models for human walking and running in hardware, our lab intends to design and construct a human-like planar biped. For safety and cost reasons, we design the robot to be at half scale to a full human, with a reduced mass of 20 kg. In the following sections, we describe our process for selecting our desired performance envelope and our mechanical design and control decisions for our first prototype of a biped knee actuator.

2.1 Design Constraints

To test reflexive control strategies for adult humans, our half-size robot must be dynamically similar to a full-size human. We achieve this through dimensional analysis as described in [15]. Our system is specified as a mass-length-time (MTL) system. We have already specified our target leg length and mass, L=0.5 m and M=20 kg, and given that gravity remains constant, we must solve (rather than select) for t. These fundamental quantities are shown in Table 1. We use these fundamental quantities to derive scale factors for important physical variables shown in Table 2 that we will use in subsequent sections.

Table 1: Fundamental Quantities for Dimensional Analysis

Fundamental Quantity	Scaling Factor
Length (L)	1/2
Mass (M)	1/4
Gravity (g)	1

Table 2: Physical Variable Scale Factors

Physical Variable	Scale	Scale Factor
Force (F)	M	1/4
Torque (T)	ML	1/8
Time (t)	$\sqrt{L/G}$	$1/\sqrt{2}$
Velocity (V)	L/t	$1/\sqrt{2}$

As mentioned previously, our whole-biped target mass is 20 kg with a 0.5 m leg length. We acquire standard human limb lengths and masses from [14]. Scaled limb lengths and masses appear in Table 3.
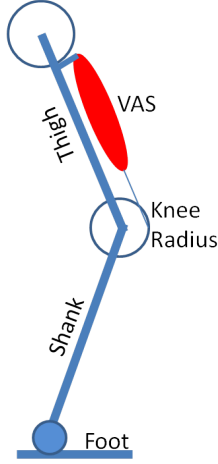
Figure 5: Simple leg model showing vastus group and pulley-like knee structure

Table 3: Biped Limb Lengths and Masses

Property	Full Human	Half-Scale Biped
Leg Length (m)	1	.5
Thigh Length (m)	.46	**.23**
Shank Length (m)	.54	.27
Knee Radius (m)	.06	**.03**
Biped Mass (kg)	80	20
Thigh Mass (kg)	8	**2**
Shank Mass (kg)	3.7	.9
Foot Mass (kg)	1.2	.3

Ideally, the robot's joint dynamics will perform as well or better than a half-scaled human. This goal poses a challenge for actuation, as the actuators must deliver human-comparable joint torques and speeds while meeting strict weight and size requirements. In this paper, we focus specifically on the design of the actuator for the knee joint extensor. In humans, the performance envelope for the knee extensor is dominated by the vastus muscle complex located in the front of the thigh. Thus, we derive our actuator requirements by setting our desired no-load speed to the maximum contraction velocity of the scaled vastus complex, and our target operating torque to be equal to the maximum knee joint torque estimated for the torques developed by the scaled vastus complex. We calculate

the maximum knee joint torque by multiplying the muscle complex's maximum isometric force by the scaled knee joint radius given in Table 3. We reference our muscle data from [12]. Our joint torque and speed requirements can be seen in Table 4. Extracting relevant knee joint information allows us to summarize our actuator requirements in Table 5.

Table 4: Muscle and Joint Properties for the Vastus Complex

Property	Full Human	Scale Factor	Half-Scale Biped
Max. Isometric Force (N)	6000	1/4	1500
Max. Velocity (m/s)	.96	$1/\sqrt{2}$	.68
Max. Joint Torque (Nm)	360	1/8	45
Max. Joint Speed (rpm)	153	$(1/\sqrt{2})/(1/2)$	217

Table 5: Knee Actuator Design Specifications

Actuator Property	Target
Speed	217 rpm
Torque	45 Nm
Mass	<2 kg
Size	$<23{\times}10{\times}8$ cm^3

2.2 Drive Train Design Choices

We wish for any technology developed through this robot to be easily transferrable to prosthetic and orthotic devices. Hydraulic and pneumatic actuators, commonly used in other high performance legged systems, cannot be used in our research because they require massive hardware components such as pumps and accumulators and typically generate a level of noise that makes them unacceptable for wearable technology. Instead, we choose electric motors as our primary method of actuation for their low audible noise, compactness, and availability in many different form factors and power ratings. In order to choose appropriate motors, we assume stiff actuation and high efficiency. We limit our selection to Maxon's RE line of high-quality brushed DC motors. The only single motor which will meet our power requirements is the 250-watt RE-65, which immediately exceeds our weight limit of 2 kg. As an alternative solution, we choose to design our actuator around two RE-40 motors geared in parallel, which yield a combined power

of 300 watts at a combined mass of 960 g. We also find that other combinations of multiple motors can yield similar power at lower weight. Table 6 compares three exmaples, of which an arrangement of four RE-30 motors is shown to have improved weight and rotor inertia. In order to limit mechanical complexity and to test the feasibility of parallel geared motors, however, we use only two RE-40 DC motors in our initial prototype. As will be shown, two RE-40 motors easily fit within our specified size envelope while leaving space for the compliant element, gearing, and sensors.

Table 6: Multi-Motor Comparisons

Un-Geared Single Motor	RE-65	RE-40	RE-30
Power Ea. (W)	250	150	60
Weight (g)	2100	480	238
Rotor Inertia (gcm^2)	1340	138	34.5
Nom. Torque (mNm)	679	184	88.2
Nom. Speed (rpm)	3340	7000	7750
Stall Torque (mNm)	16600	2500	1020
No Load Speed (rpm)	3550	7580	8490
Geared Motor Cluster	**1x RE-65**	**2x RE-40**	**4x RE-30**
Number	1	2	4
Gear Ratio	17	36	40
Total Power (W)	250	300	240
Total Weight (g)	2100	960	952
Ref. Rotor Inertia (kgm^2)	**0.0387**	**0.0358**	**0.0221**
Nom. Torque (Nm)	**11.5**	**13.2**	**14.1**
Nom. Speed (rpm)	196	194	194
Stall Torque (Nm)	282	180	163
No Load Speed (rpm)	**209**	**211**	**212**

In order to reach our target joint velocity of 217 rpm, we require a gear ratio of 36:1. The stock planetary gearboxes for the RE-40s weigh more than 360 g each and add considerable length to the motors, while an additional gear stage is necessary to couple both motors together. Harmonic drives are compact, but are similarly massive as compared with planetary gearboxes at approximately 500 g for a transmission appropriate to our actuator specifications. This limitation forces us to build our own gearboxes. Because the proposed leg design is cable driven, we are able to use a smaller output pulley on the actuator to achieve a final reduction stage of 3:1 from the actuator to the knee joint. This reduces the

required internal gear ratio of the actuator to 12:1. The internal gearing consists of two stages: a 4:1 spur gear set that joins the two motors, and a 3:1 bevel gear pair to properly orient the axis of rotation. These gear stages are shown in Figure 6.
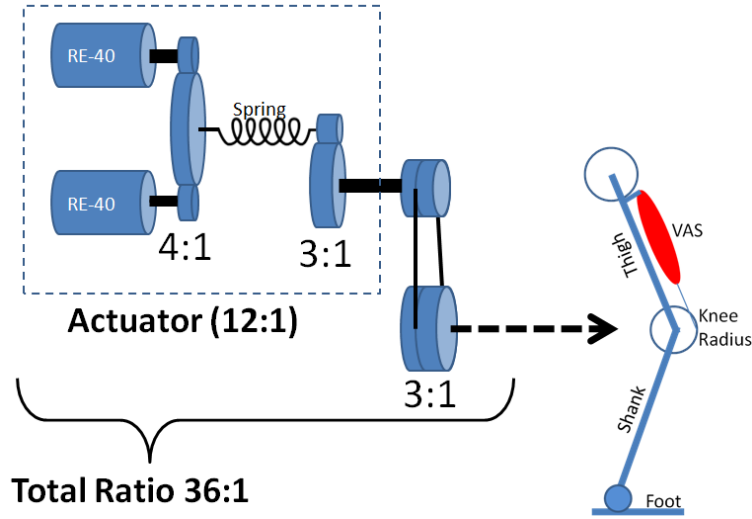

Figure 6: Diagram of Mechanical Transmission

Typically, the elastic element for a SEA is located at the interface between the load and the final gear stage, but in order to remain within our specified size envelope, we opt to locate a rotary spring coupling between the internal 4:1 and 3:1 gear stages. This decision also enables us to use a lighter spring, as the maximum torque applied will be reduced by the 9:1 gear ratio from elasticity to load. While we intend to explore custom spring couplers in the future, for now we choose an off-the-shelf spring coupler from Stock Drive Products with a spring stiffness of 1.75 Nm/rad. and a maximum torque rating of 1.4 Nm. Due to gearing, this corresponds to a stiffness of 5.25 Nm/rad and a maximum torque of 4.2 Nm. at the actuator output. Likewise, the knee joint will then have a stiffness of 15.75 Nm/rad. and a maximum torque rating of 12.6 Nm. This is less than our initial torque specification, but it provides sufficient torque capacity for our research group's initial swing-leg experiments. The actuator has been designed with ample space for a more robust spring to be used in the future, as shown in Figure 7.
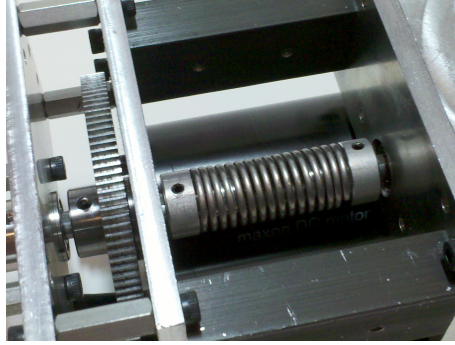
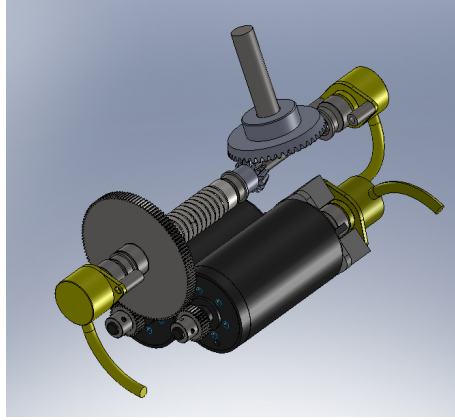Figure 7: Photo of the elastic element inside the actuator

Figure 8: Mechanical transmission without frame, showing two motors, both gear stages, and intermediate elasticity

To meet the size constraints of the actuator, the internal transmission is arranged as shown in Figure 8. We design the frame for the actuator to be as lightweight and simple as possible while still being capable of withstanding the torques and forces expected from the knee joint. The original design is shown in Figure 9a. In order to reduce machining time and cost for the first prototype, the more basic design shown in Figure 9b has been constructed.

(a) Pre-fabrication concept of compact actuator

(b) Final actuator design, simplified for low-cost fabrication
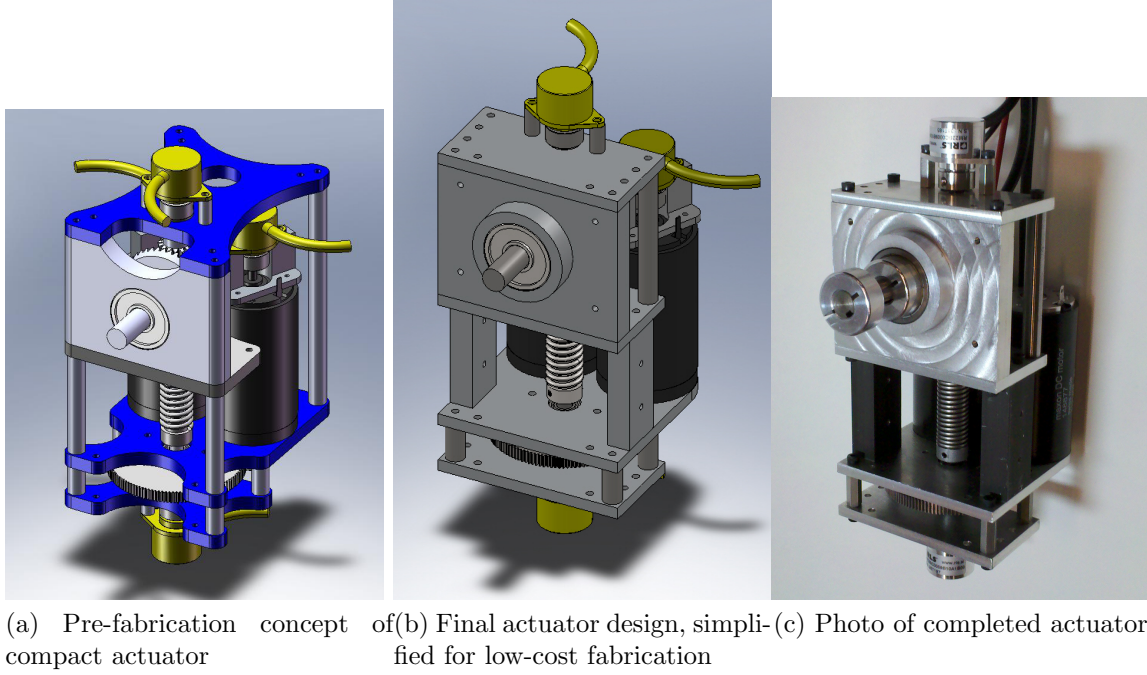
(c) Photo of completed actuator

Figure 9: Actuator Design Iterations

The fabricated actuator is shown in Figure 9c. The actuator weighs approximately 1.7 kg, which leaves 300 grams for the remaining leg structure. On future revisions, we will reduce the thickness of the support plates and remove additional material using patterns similar to those in Figure 9a.

Table 7 compares he actuator specifications with our design goals. We have met both our size and weight goals, and our no-load speed is effectively matched to our target velocity identified from the maximum contractile velocity of the half-scaled vastus complex. While the nominal torque does not reach the corresponding goal calculated from the maximum isometric force of the scaled vastus complex, this torque would only be necessary for short durations during the extremes of dynamic behavior. For these short periods of time, we anticipate that we will be able to overdrive the motors to reach the necessary torque. At the moment, however, we are limited by our compliant element's breaking strength.

Table 7: Actuator Specifications

Specification	Target	Actual
Dimensions (cm^3)	$23 \times 10 \times 8$	$20.5 \times 9.5 \times 8$
Weight (kg)	< 2 kg	1.8
Nom. Torque (Nm)	45	13
Stall Torque (Nm)	—	180
No Load Speed (rpm)	217	210
Spring Stiffness (Nm/rad)	—	1.75
Output Stiffness (Nm/rad)	—	15.75

3 Series-Elastic Control

We implement and compare two control architectures to achieve high-bandwidth actuator force control. Both of these methods include compensation using inverse process dynamics and PID control. Our first method is an implementation of the torque-embedded control proposed by Pratt and Williamson [1]. Our second method is a new velocity-embedded approach. We suggest that the velocity-embedded approach provides significant advantages by rejecting gear inefficiencies and motor nonlinearities without the requirement of known load dynamics present in previous velocity-based control methods. In our explanations of each approach, we will use the following variable definitions from Table 8.

3.1 Torque-Embedded Control

The derivation for torque-embedded control matches that which appears in [1], except that we use rotational units rather than linear units. In order to formulate the torque-based actuator model, we begin with the equation for the angular deflection of the spring according to Hooke's law

$$T_l = -k_s(\theta_l - \theta_m). \tag{1}$$

We know that the rotor acceleration of the dc motor is given by the sum of torques acting on the rotor divided by its rotational inertia. The two torques acting on the motor are the motor winding torque T_m and torque from the spring, which is equal to the torque applied to the load, T_l. If we integrate the acceleration twice, we have an expression for the motor position

Table 8: Control Variable Definitions

Variable	Symbol
Load Torque	T_l
Desired Load Torque	T_d
Motor Winding Torque	T_m
Desired M. Winding Torque	T_{dm}
Load Encoder Angle	θ_m
Motor Encoder Angle	θ_l
Load Encoder Velocity	ω_m
Motor Encoder Velocity	ω_l
Motor Rotational Inertia	J_m
Load Rotational Inertia	J_l
Actuator Spring Constant	k_s
Gear Ratio, Motor to Spring	n_m
Gear Ratio, Spring to Load	n_l
Current Control Time Constant	t_c
Velocity Control Time Constant	t_v

$$\theta_m = \frac{T_m - T_l}{J_m s^2}. \tag{2}$$

Combining these equations yields a function relating motor torque to the torque of the actuator

$$T_m = T_l + \frac{J_m}{k_s} s^2 T_l + J_m s^2 \theta_l. \tag{3}$$

For the moment, we assume that our current controller is perfect and there are no nonlinearities in the motor, e.g. $T_m = T_{dm}$. Our goal is to find a solution for T_{dm} such that $T_l = T_d$. We substitute T_d for T_l and solve for T_{dm}

$$T_{dm} = T_d + \frac{J_m}{k_s} s^2 T_d + J_m s^2 \theta_l. \tag{4}$$

16

The three terms in this equation represent, in respective order: the steady-state motor torque required to exert a fixed torque on the load, the motor torque required to accelerate the motor inertia to achieve a deflection of the spring and a change in load torque, and the torque required to accelerate the motor inertia to track the rotation of the load. When summed together, these three terms capture the inverse dynamcis of the ideal model. If the modeled system is geared with a ratio of n_m from motor to spring and n_l from spring to load, we can alter our model with the substitutions shown in Table 9, which describe how motion, torque, and inertia are reflected through these gear stages.

Table 9: Substitutions to Account for Gearing

No Gearing	Geared
T_d	$\dfrac{T_d}{n_l}$
T_{dm}	$T_{dm}n_m$
J_m	$J_m{n_m}^2$
J_l	$\dfrac{J_l}{{n_l}^2}$
$\theta_m{}^*$	$\dfrac{\theta_m}{n_m}$
$\theta_l{}^*$	$\theta_l n_l$
$\omega_m{}^*$	$\dfrac{\omega_m}{n_m}$
$\omega_l{}^*$	$\omega_l n_l$

The substitutions labeled with an asterisk in Table 9 should only be made if the encoders are located at the motor and/or load. In the case of our actuator, the encoders are located at either end of the spring, so these substitutions are not made in the formulation of our specific case. Thus, equation 4 becomes

$$T_{dm}n_m = \frac{T_d}{n_l} + \frac{J_m{n_m}^2}{k_s}s^2\frac{T_d}{n_l} + J_m{n_m}^2 s^2\theta_l. \tag{5}$$

The block diagram of the inverse process dynamics terms and the plant are illustrated in Figure 10, along with the PID controller $P(s)$ for error correction. The transfer function $C(s)$ represents the current controller, which in many cases can be modeled as a simple low-pass filter [18].
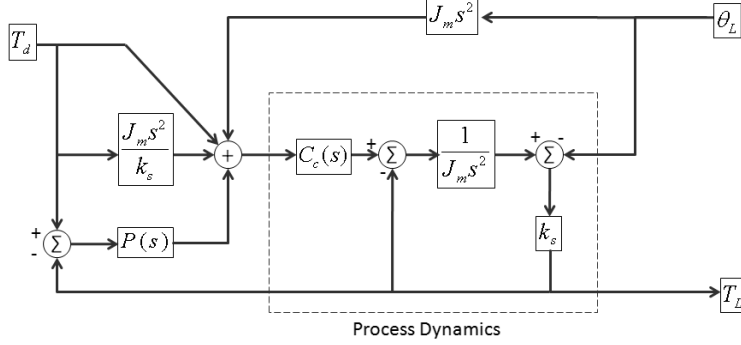
Figure 10: Torque-embedded control as proposed by Pratt and Williamson [1][8]

To analyze the closed-loop response of the entire system for various load conditions, we present the transfer functions for a system with no gearing. The general function simplifies to

$$\frac{T_l}{T_d} = \frac{P(s)k_s + J_m s^2 + k_s}{P(s)k_s + J_m \left[\dfrac{1}{C(s)} - L(s)k_s(1 - \dfrac{1}{C(s)})\right]s^2 + \dfrac{k_s}{C(s)}}. \tag{6}$$

where the transfer function $L(s) = \dfrac{\theta_l}{T_l}$ describes general load dynamics. We can assume a simple model of our controller as a low-pass filter with time constant t_c

$$C(s) = \frac{1}{t_c s + 1}. \tag{7}$$

Given this controller model, the transfer function becomes

$$\frac{T_l}{T_d} = \frac{P(s)k_s + J_m s^2 + k_s}{P(s)k_s + J_m\left[t_c s + 1 - L(s)k_s t_c s\right]s^2 + k_s(t_c s + 1)} \tag{8}$$

$$= \frac{P(s)k_s + J_m s^2 + k_s}{P(s)k_s + J_m t_c\left[1 - L(s)k_s\right]s^3 + J_m s^2 + k_s t_c s + k_s}. \tag{9}$$

Let us first assume an inertial model for our load dynamics

18

$$L(s) = \frac{1}{J_l} s^2. \tag{10}$$

Then, the transfer function then becomes

$$\frac{T_l}{T_d} = \frac{P(s)k_s + J_m s^2 + k_s}{P(s)k_s + J_m t_c s^3 + J_m s^2 + k_s t_c (1 - \frac{J_m}{J_l})s + k_s}. \tag{11}$$

As the load inertia J_l becomes very large, the system approaches

$$\frac{T_l}{T_d} = \frac{P(s)k_s + J_m s^2 + k_s}{P(s)k_s + J_m t_c s^3 + J_m s^2 + k_s t_c s + k_s}. \tag{12}$$

which is identical to the fixed-output case where the actuator shaft is held still. We will use this condition in section 5 to compare control methods.

For a typical motor controller, we can expect a current bandwidth of a few kHz, which corresponds to a time constant on the order of a few tenths of a millisecond. This model makes the assumption that internal torques due to friction and damping between the gears are negligible. For a direct-drive case, this is a reasonable assumption. Additionally, as can be clearly seen from the block diagram, two of the compensating inverse dynamics terms require second-order differentiation, which will require the desired torque T_d and the position signal θ_l to be filtered to smooth step changes and remove noise. These filters will impose additional bandwidth limitations on the system.

3.2   Velocity-Embedded Control

As an alternative, we propose a similar control system with inverse dynamics compensation, but with a commanded motor velocity rather than current. We again start with the equation for the torque exerted by the spring due to angular deflection

$$T_l = -k_s(\theta_l - \theta_m). \tag{13}$$

This time, instead of substituting an equation with motor torque T_m and inertia J_m for θ_m, we use motor velocity ω_m

19

$$\theta_m = \frac{\omega_m}{s}. \tag{14}$$

This leads to the expression for motor speed as a function of the load torque T_l

$$\omega_m = \frac{T_l}{k_s}s + \theta_l s. \tag{15}$$

As before, we assume a perfect controller (this time for velocity rather than torque) and solve for ω_{dm} as a function of T_d

$$\omega_{dm} = \frac{T_d}{k_s}s + \theta_l s. \tag{16}$$

If we include gear ratios and place the encoders at the motor and output, this becomes

$$\frac{\omega_{dm}}{n_m} = \frac{T_d}{n_l k_s}s + \theta_l n_l s. \tag{17}$$

The block diagram for our proposed control architecture can be seen in Figure 11. Note that the two terms that use the inverse process dynamics are only single differentiators. This should require less sensor and control signal filtering than torque-embedded control, which uses second-order derivatives.
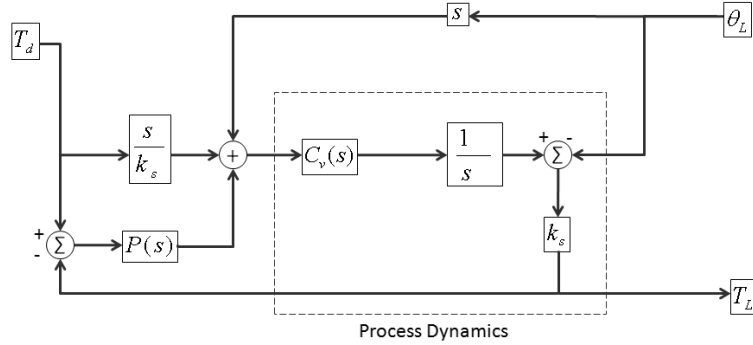

Figure 11: Our proposed velocity-embedded control method

Solving for the system transfer function, we find

20

$$\frac{T_l}{T_d} = \frac{P(s)k_s + s}{P(s)k_s + (\frac{1}{C(s)} - L(s)k_s(1 - \frac{1}{C(s)}))s}. \tag{18}$$

As with torque-embedded control, if $C(s) = 1$, i.e. perfect velocity control, the transfer function simplifies to 1. We assume again that our controller acts as a low-pass filter with time constant t_v. In this case, because we are using velocity control, we can expect this time constant to be larger than the one for current control, as velocity control is wrapped around current control within the amplifier. A typical servo amplifier will have a velocity control bandwidth of a few hundred Hz, corresponding to a time constant of a few milliseconds. The exact response will have a dependency on motor inertia, though this can be empirically determined by observing the rise time of a commanded step change in velocity. With this controller model, our transfer function becomes

$$\frac{T_l}{T_d} = \frac{P(s)k_s + s}{P(s)k_s + [t_v - L(s)k_s]\, s^2 + s}. \tag{19}$$

For the inertial load model $L(s) = \frac{1}{J_l}s^2$, this becomes

$$\frac{T_l}{T_d} = \frac{P(s)k_s + s}{P(s)k_s + t_v s^2 + s - \frac{k_s}{J_l}}. \tag{20}$$

When the load inertia becomes very large, the transfer function approaches

$$\frac{T_l}{T_d} = \frac{P(s)k_s + s}{P(s)k_s + (t_v s + 1)s}. \tag{21}$$

Like the torque-embedded control architecture proposed by Pratt and Williamson[1], our velocity-embedded control method is limited primarily by the time constant of our motor controller. While a typical time constant for velocity control may be an order of magnitude longer than a typical time constant for current control, our novel approach offers several key benefits. First, the control designer does not need to have a precise estimate for motor inertia. Second, losses due to gear dynamics between the motor and spring need not be considered, as the velocity loop automatically compensates for these losses without additional tuning of the outer control loop. Third, the inverse dynamics terms still have differentiators, but

because they require only single-order differentiation, they work well with faster low-pass filters leading to increased overall system bandwidth. Fourth, to achieve steady-state error, the motor needs only to match the velocity of the load, which reduces the need for a significant integral term in the PID controller. Finally, a key advantage of our method for velocity-embedded control over the method proposed by [3] is that it does not need to assume a known load inertia, instead allowing for general load dynamics in the form of $L(s) = \dfrac{\theta_l}{T_l}$.

4   Simulation and Implementation

We determine PID gains by testing our specific actuator under a fixed-load condition where the output does not move. This is functionally identical to the case where the actuator is coupled to a massive load. Because our test harness cannot withstand the high torques generated by the actuator, we command smaller torques using only one of the two available motors. The physical parameters of our actuator are given in Table 10.

Table 10: Actuator Control Parameters

Property	Value
J_m	1.3×10^{-5} kgm^2
k_s	1.75 Nm/rad
n_m	4
n_l	9
t_c	6.4×10^{-5} s
t_v	4.5×10^{-4} s

4.1   Torque-Embedded Control Results

Modeling the process dynamics from Figure 10 yields the transfer function

$$\frac{T_l}{T_{dm}} = \frac{n_l n_m k_s}{(t_c s + 1)(n_m{}^2 J_m s^2 + k_s)}. \tag{22}$$

Substituting the actuator parameters from Table 10 yields process dynamics with the frequency response shown in Figure 12. The spike in amplitude indicates the theoretical resonant frequency of the spring and motor inertia.
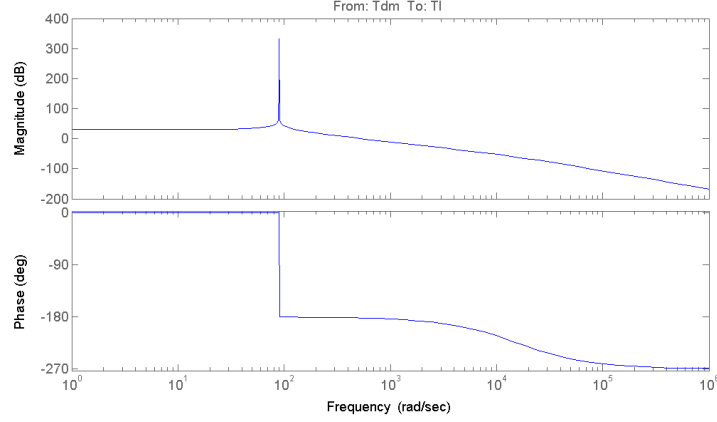
Figure 12: Torque-embedded process dynamics using the values specified in Table 10

Because we are testing the actuator using a fixed load, the torque-embedded system transfer function simplifies to

$$\frac{T_l}{T_d} = \frac{P(s)k_s + J_m s^2 + k_s}{P(s)k_s + J_m t_c s^3 + J_m s^2 + k_s t_c s + k_s}. \tag{23}$$

Our motor controllers (Solo Whistles from Elmo Motion Control) have a specified current bandwidth of $2.5kHz$, which corresponds to a time constant t_c of about $6.4e^{-5}$ seconds. We use absolute magnetic encoders (Renishaw model RM-22) to measure the load-side and motor-side angular position of the spring, which we then use to calculate spring deflection as a difference of the two angles. The analog encoder signals are filtered in software with a cutoff frequency of 30 Hz. Likewise, each derivative is paired with a low-pass filter of 30 Hz. This frequency is chosen to diminish the effects of noise without slowing the system response.

We begin tuning the PID controller by setting the integral and derivative terms to zero and disabling the feedforward and inverse dynamics terms. We increase the proportional gain until the step response begins to overshoot. We then increase the derivative gain and the proportional gain together to decrease the rise time without causing errors or oscillations. Finally, we increase the integral gain to reduce steady state error and further decrease the response time of the system. After these initial gains are selected, we add in the feedforward and inverse dynamics terms and manually tune the PID gains until the fastest system response is reached with little overshoot.
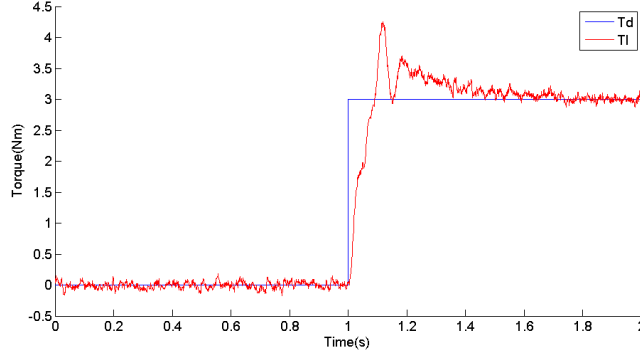
23

Figure 13: Observed step response for torque-embedded control: P=0.2 I=P/.05 D=0.05P. Torque is limited to 3 Nm in our tests for safety reasons.

As is shown in Figure 13, the rise time achieved with torque-embedded control is approximately 100 ms with approximately 30% overshoot. While the steady-state behavior of the system contains zero error apart from noise, the step response suggests that this control method may not be fast enough for biomimetic motions such as walking or running. We see from Figure 14 that the controller lags by approximately 50 ms at 2 Hz. Attempts at higher PID gains result in instability and unacceptable levels of overshoot.
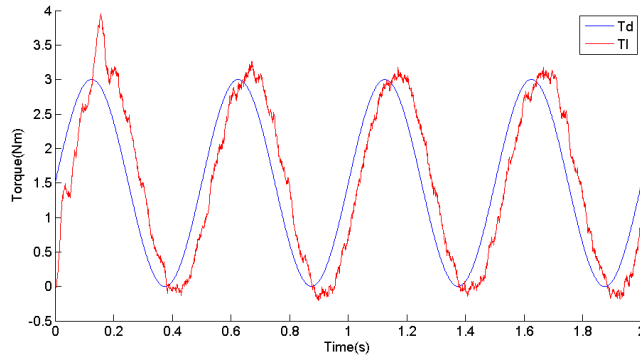

Figure 14: Sine response at 2 Hz for torque-embedded control: P=0.2 I=P/.05 D=0.05P

If we examine the frequency response of the fixed-load transfer function for the PID gains we have chosen, shown in Figure 15, we see that we should be able to accurately track torque commands up to 1000 rad/s, or 160 Hz. Our experimental

results, however, show that we can only accurately track torque commands up to 10 rad/s, or 1.6 Hz.
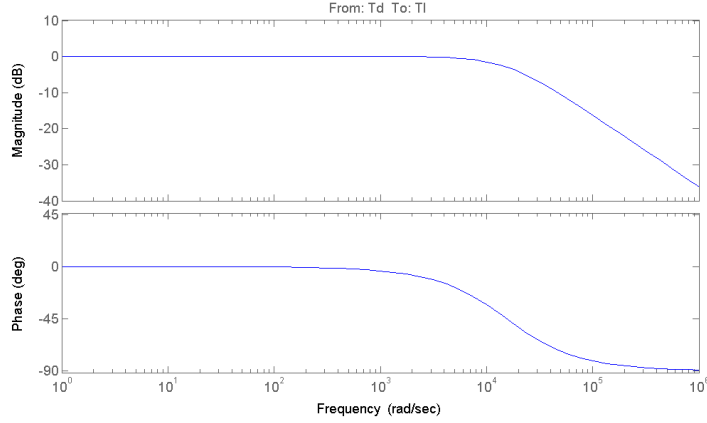

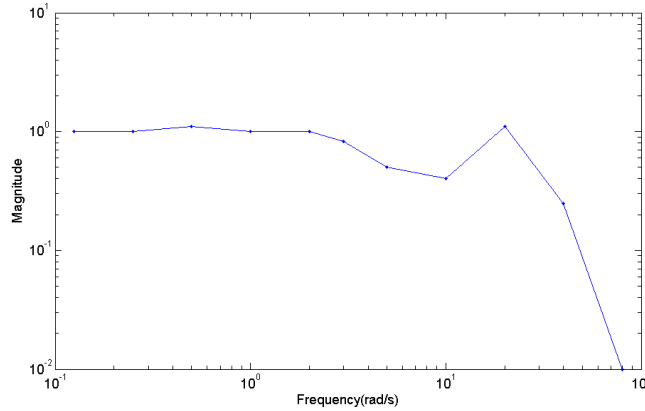Figure 15: Transfer function frequency response for torque-embedded control: P=0.2 I=P/.05 D=0.05P

Figure 16: Measured frequency response for torque-embedded control: P=0.2 I=P/.05 D=0.05P

We believe that the low performance of this control scheme is caused primarily because of noise and uncertainty in the encoder signals. The second-order differentiators in the feedforward and inverse dynamics terms become ineffective or even detrimental to the response of the control system. The filtering necessary

to achieve very clean signals from these terms introduces unacceptable delays for nominal biomimetic operating frequencies 2 Hz and higher frequencies near 20Hz for disturbances. Additionally, the steady-state behavior of the system relies on a well characterized motor current constant and spring constant. While we trust our motor to perform as specified, the spring coupler appears to suffer from hysteresis and is also approximately four times stiffer than specified in the datasheet. The spring's uncertain behavior means that the steady-state term in the controller will not necessarily result in zero error.

4.2   Velocity-Embedded Control Results

Modeling the process dynamics from Figure 11 yields the transfer function

$$\frac{T_l}{\omega_{dm}} = \frac{n_l k_s}{n_m s(t_v s + 1)}. \tag{24}$$

Substituting the actuator parameters from Table 10 yields process dynamics with the frequency response shown in Figure 17. Note that the system lacks the resonant frequency seen in Figure 12, as the velocity control loop around the motor will keep its motion bounded.
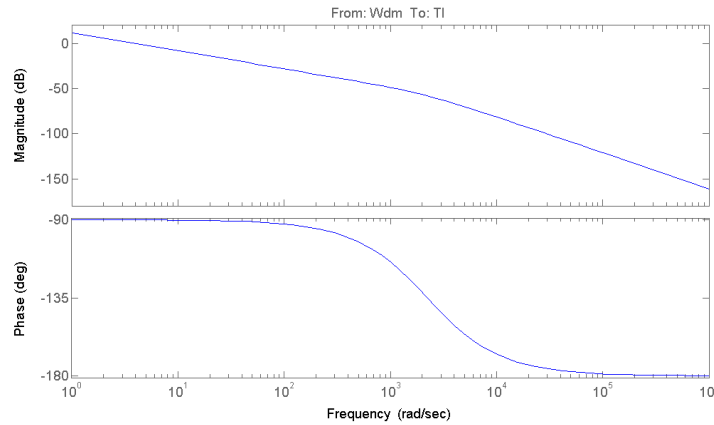

Figure 17: Velocity-embedded process dynamics using the values specified in Table 10

Again, we determine PID gains by testing our actuator under a fixed-load condition. The relevant transfer function for velocity-embedded control is given as

$$\frac{T_l}{T_d} = \frac{P(s)k_s + s}{P(s)k_s + (t_v s + 1)s}. \tag{25}$$

We need only the spring constant k_s and the velocity control loop time constant t_v for the Solo Whistle controller from Table 10. The velocity bandwidth is 350 Hz, which corresponds to a time constant t_v of about 4.5×10^{-4} s. Note that this is an order of magnitude slower than the Solo Whistle's current-control time constant of 6.4×10^{-5} s. For velocity-embedded control, we use only PD gains, as integral control is not needed to achieve zero steady-state error.
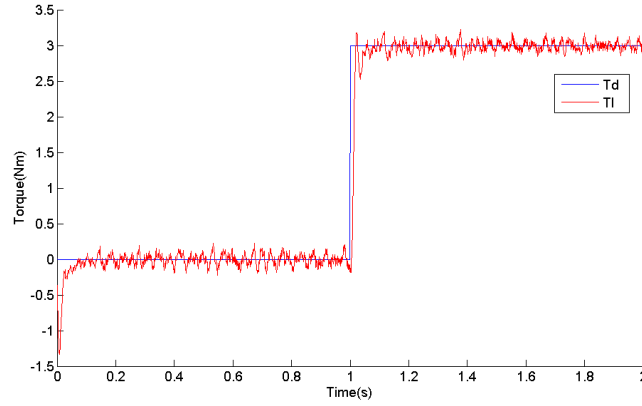

Figure 18: Observed step response for velocity-embedded control: P=1000 I=0 D=P*.0001

From the step response shown in Figure 18, we see that the system with our chosen PD gains has a rise time of approximately 15 ms, which is nearly an order of magnitude faster than our torque-embedded control. Similarly, in Figure 19, we see that velocity-embedded control tracks a 2 Hz torque command with a delay of approximately 5 ms.
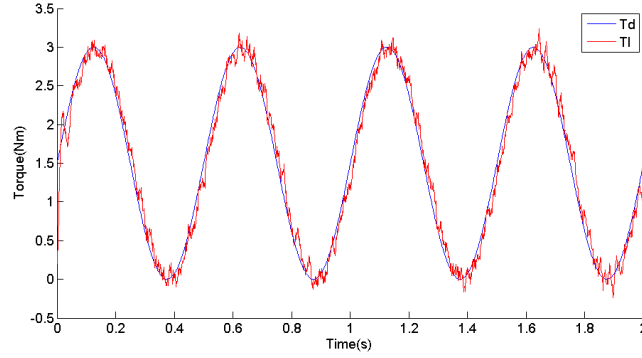
Figure 19: Sine response at 2 Hz for torque-embedded control: P=1000 I=0 D=P*.0001

The transfer function bode plot (Figure 20) predicts similar performance compared to torque-embedded control, with the system's cutoff frequency at approximately 1000 rad/s, or 160 Hz. Again, our actual measured performance falls short of this prediction, but velocity-embedded control can accurately track torque commands up to 100 rad/s (16 Hz), which is an order of magnitude higher than our implementation of torque-embedded control, as shown in Figure 21.
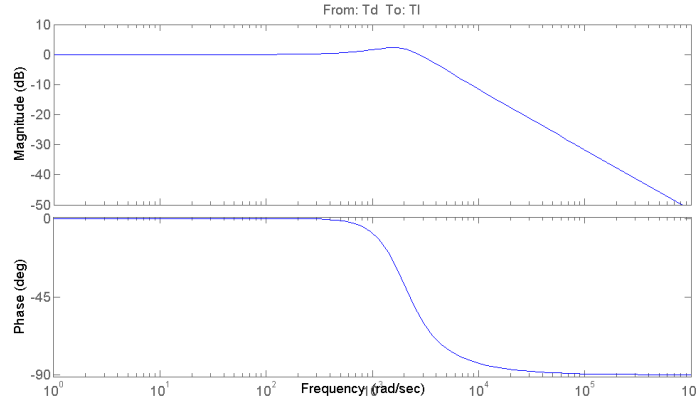

Figure 20: Transfer function frequency response for velocity-embedded control: P=1000 I=0 D=P*.0001
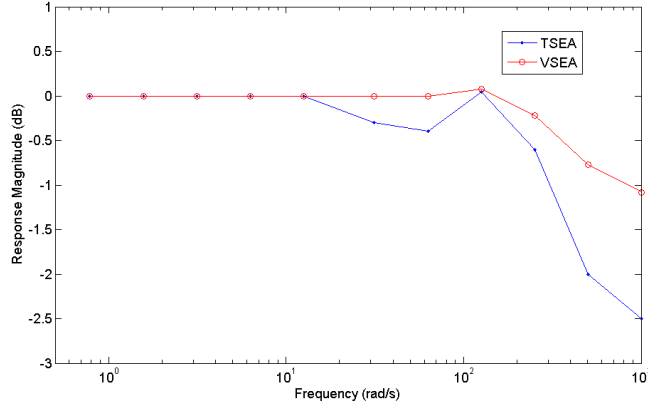
Figure 21: Measured frequency response for velocity-embedded control and torque-embedded control. With the exception of the resonant peak at 10^2 rad/s, velocity-embedded control accurately tracks higher frequencies by an order of magnitude.

Our results show that our velocity-embedded control method improves the torque bandwidth of our actuator by a factor of ten. The improved performance is the result of two primary factors. First, the inner velocity loop eliminates the need for precise knowledge of motor inertia, gear dynamics, and motor torque/current relationships. Second, the first-order feedforward and inverse dynamics terms are more robust to high-frequency disturbances such as encoder noise and step changes in commanded torques, as compared with the second-order differentiators used in torque-embedded control.

5   Discussion and Conclusions

In this paper, we have demonstrated the design, construction, and control of a multi-motor series-elastic actuator for a robotic knee. Our actuator is designed to match the performance of the vastus muscle group, dynamically scaled for a half-size biped. We show that we can effectively command torques from the actuators using deflection feedback from our elastic element. Our proposed velocity-embedded control architecture offers several key advantages over traditional torque-embedded control, including intrinsic compensation for gear dynamics and greater immunity to noisy signals from sensors and higher-level controllers. This yields high-bandwidth torque control, especially in the presence of noisy feedback signals and unknown actuator dynamics in the gears and motor.

During testing, we identified several potential areas of improvement for the mechanical design of the actuator. First among these is the need for a different spring coupler. While the off-the-shelf couplers we used were very convenient for our initial prototype, they proved to be four times as stiff as specified in the datasheet. For future prototypes, we will seek more compliant springs which are also rated for higher maximum torques than our current spring couplers. These springs will likely require custom fabrication. Additionally, we observe a spring hysteresis of approximately 0.25 Nm around zero torque, which hinders our ability to command low actuator impedances. In the future, a compliant element with a nonlinear stiffness may improve performance with low stiffness for small deflections and larger stiffness for large deflections. The current hysteretic behavior may also be caused partly by the acetal bevel gears between the spring and the output. We plan to replace these with steel gears which should resist the wear we see on the acetal gears in the presence of high torques. Finally, our analog encoders introduce a significant amount of noise and uncertainty into the control system, and our control response is made slower by the filtering necessary to extract useful spring deflection information. The current revision uses analog encoders with an internal 9-bit digital to analogue conversion. We plan to replace these with 13-bit digital encoders, which will both significantly increase resolution and decrease the effects of noise. Finally, we believe that future revisions of the actuator can be made lighter than our current revision, and that this research will enable us to build full bipeds using the design principles outlined in this paper.

5.1 Future Directions

In order to further validate both controllers, we plan to test the actuator using simulated joint trajectories in the coming weeks. We will do this first by coupling the actuator to a much larger position-controlled motor. We will also use the actuator to control the joint trajectory of one leg of the half-size biped. Also, while we will not likely need the actuator's full power for our initial swing-leg testing, we plan to utilize both parallel motors for future experiments. Our initial approach will be to wire both motors in series off of a single motor controller. In this way, both motors will be exerting torque in the same direction at all times. We should be able to achieve twice the torque, however, our motor controller will also need to be able to source twice the voltage that would normally be used for only one motor.

Our current design meets our power requirements for proposed swing-leg testing while meeting size and weight limits, but this leaves only 300 grams for the remaining leg structure. The motors account for nearly two thirds of the total actuator weight. We plan to investigate the possibility of replacing one of our two

motors with a clutched spring in parallel with the remaining motor, as shown in Figure 22. The spring would serve as an energy storage device that can reduce the torque load on the motor for motions that pull on the motor. Upon the biped's leg contacting the ground, for example, we would engage the spring so that as the leg compresses, it stores energy in the spring which will assist the motor during extension. During swing phase, we would disengage the spring so that it does not act against the motor. Initial concept sketches suggest that the parallel spring could fit within the existing volume of one motor while weighing no more than 100g. Additionally, energy savings for a simple reflexive hopping robot could be as high as 90% [13].

Given the hysteretic problems we observe from our current compliant element and the large range of torques we wish to command, we plan to investigate non-linear springs as a potential improvement to the actuator's mechanical design. In addition to specifying the force-length relationship for the performance benefits we expect from being able to measure small and large deflections with improved resolution, we will design the springs to be analogous to the nonlinear stiffness of biological tendons.
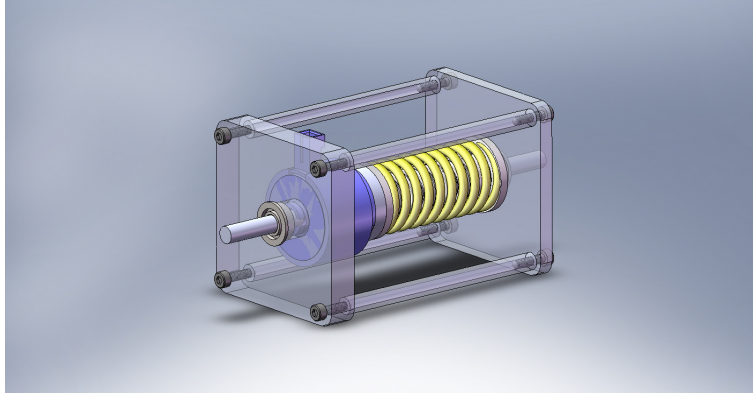

Figure 22: Concept for concentric clutch mechanism for series and parallel elasticity. The series spring is located inside of the larger spring. The larger spring is grounded at one end and connected to the clutch at the other. Upon clutching, the large outer spring engages the drive train and stores energy as it is deflected.

References

[1] G.A. Pratt, M.M. Williamson, "Series elastic actuators," Intelligent Robots and Systems, IEEE/RSJ International Conference on, p. 399, International Conference on Intelligent Robots and Systems-Volume 1, 1995

[2] G. A. Pratt et al. "Late motor processing in low-impedance robots: Impedance control of series-elastic actuators." In *Proceedings of the 2004 American Control Conference*, 2004.

[3] G. Wyeth. "Control issues for velocity sourced series elastic actuators." In *Proceedings of Australasian Conference on Robotics and Automation 2006*, 2006.

[4] G. Wyeth. "Demonstrating the safety and performance of a velocity sourced series elastic actuator." In *IEEE International Conference on Robotics and Automation*. 2008

[5] Kong, K., Bae, J., and Tomizuka, M., " Control of Rotary Series Elastic Actuator for Ideal Force- Mode Actuation in HumanRobot Interaction Applications, *IEEE/ASME Trans. on Mechatronics*, 2009 Vol. 14, No. 1, pp. 105 118.

[6] D.W. Robinson et al, "Series Elastic Actuator Development for a Biomimetic Walking Robot." *IEEE/ASME International Conference on Advanced Intelligent Mechatronics*, 1999. p561

[7] J.W. Hurst, D. Hobbelen, and A. Rizzi. "Series Elastic Actuation: Potentials and Pitfalls." *International Conference on Climbing and Walking Robots,* 2004

[8] D.W. Robinson, "Design and Analysis of Series Elasticity in Closed-Loop Actuator Force Control." PhD thesis, Massachusetts Institute of Technology, June 2000.

[9] C.M. Chew, G.S. Hong, and W. Zhou. "Series Damper Actuator: A Novel Force/Torque Control Actuator." *Humanoids*, 2004.

[10] H. Geyer, A. Seyfarth, R. Blickhan. "Spring-mass running: simple approximate solution and application to gait stability." J Theor Biol 232: 315-328, 2005.

[11] H. Geyer, H. Herr. "A muscle-reflex model that encodes principles of legged mechanics produces human walking dynamics and muscle activities. IEEE Trans Neural Syst Rehabil Eng 18(3): 263-273, 2010.

[12] G. T. Yamaguchi et al. "A survey of human muscolutendon actuator parameters." In *Multiple Muscle Systems: Biomechanics and Movement Organization*, J. Winters and S. Y. Woo, Eds. Springer-Verlag, New York, 1990, pp. 717-778.

[13] D. Haeufle, personal communication, August 2011.

[14] D. A. Winter. "Biomechanics and Motor Control of Human Movement." John Wiley and Sons, Inc., New York, 1990.

[15] T. A. McMahon and J. T. Bonner, "On Size and Life." Scientific American Library, New York, 1983, pp. 74-78.

[16] J. W. Hurst, J. Chestnutt, and A. Rizzi, An actuator with mechanically adjustable series compliance, Robotics Institute, Carnegie Mellon University, Pittsburgh, PA, Tech. Rep. CMU-RI-TR-04-24, April 2004.

[17] Series-Elastic Actuator. Advertisement. Yobotics. Web. 18 Aug. 2011. http://yobotics.com/actuators/actuators.htm.

[18] B. Siciliano, L. Sciavicco, L. Villani, G. Oriolo, Robotics: Modelling, Planning and Control, Springer, London, 2009.